Spectrochimica Acta Part A: Molecular and Biomolecular Spectroscopy 334 (2025) 125950

Contents lists available at ScienceDirect

Spectrochimica Acta Part A:
Molecular and Biomolecular Spectroscopy

journal homepage: www.journals.elsevier.com/spectrochimica-acta-part-a-molecular-and-biomolecular-spectroscopy

Acidobasic equilibria of inubosin derivatives studied by UV–Vis spectroscopy

Thu Yen Nguyen, Mohamed Farouk Hamissa, Martin Šafařík, Petr Bouř, Jaroslav Šebestík *

Institute of Organic Chemistry and Biochemistry, Academy of Sciences, Flemingovo náměstí 2, 16610 Prague 6, Czech Republic

HIGHLIGHTS

- Dissociation constants of inubosin B derivatives.
- Semi-automatic spectra processing.
- Genetic algorithm for analysis of acidobasic and separation equilibria.

GRAPHICAL ABSTRACT

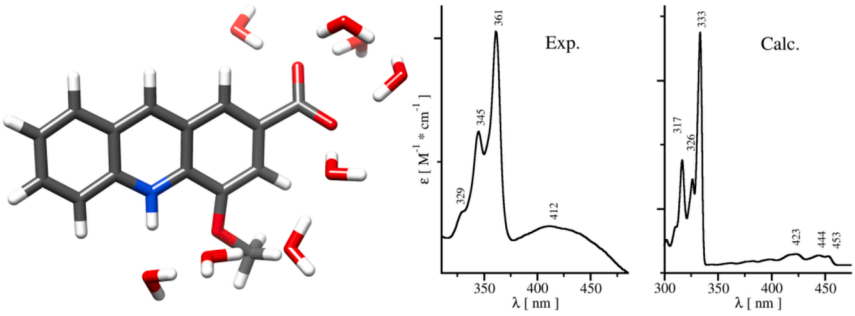

ARTICLE INFO

Keywords:
Inubosin B
Acridines
pK_a
pK_D
Absorption spectroscopy
Density functional theory

ABSTRACT

Inubosin derivatives were suggested as compounds supporting the regeneration of neurons. For practical pharmaceutical applications their physicochemical properties need to be optimized in terms of bioavailability, possible side effects, and efficiency. We focused on four inubosin B derivatives, where acidobasic constants as key players in the biological activity were determined using the UV–Vis spectroscopy. The constants were correlated with the structure on the basis of the Hammett theory. In addition, water–organic solvent equilibria were studied for selected compounds. A software for semi-automated processing of the UV–Vis titration data was developed and tested. Time dependent density functional theory (TDDFT) was used to model and interpret the experimental spectra, which made it possible, for example, to assign the most characteristic cationic band to the $S_0 \rightarrow S_2$ transition. For the acridine acid, both the TDDFT computations and the experimental data indicate that it forms zwitterion in the aqueous solution, whereas it is not dissociated in the organic phase.

Abbreviations: ACN, Acetonitrile; CPCM, Conductor-like polarizable continuum model; DFT, Density functional theory; DMSO, Dimethyl sulfoxide; ESI-MS, Electrospray ionization mass spectroscopy; EtOAc, Ethyl acetate; HOMO, The highest occupied molecular orbital; HPLC, High-performance liquid chromatography; MD, Molecular dynamics; MeOH, Methanol; minR^2, Minimal acceptable value for correlation coefficient; LUMO, The lowest unoccupied molecular orbital; ND, Neurodegenerative disease; Ngn2, Neurogenin 2; TDDFT, Time dependent density functional theory; TFA, Trifluoroacetic acid; THF, Tetrahydrofuran.

* Corresponding author.
E-mail address: sebestik@uochb.cas.cz (J. Šebestík).

https://doi.org/10.1016/j.saa.2025.125950
Received 25 November 2024; Received in revised form 18 February 2025; Accepted 23 February 2025
Available online 26 February 2025

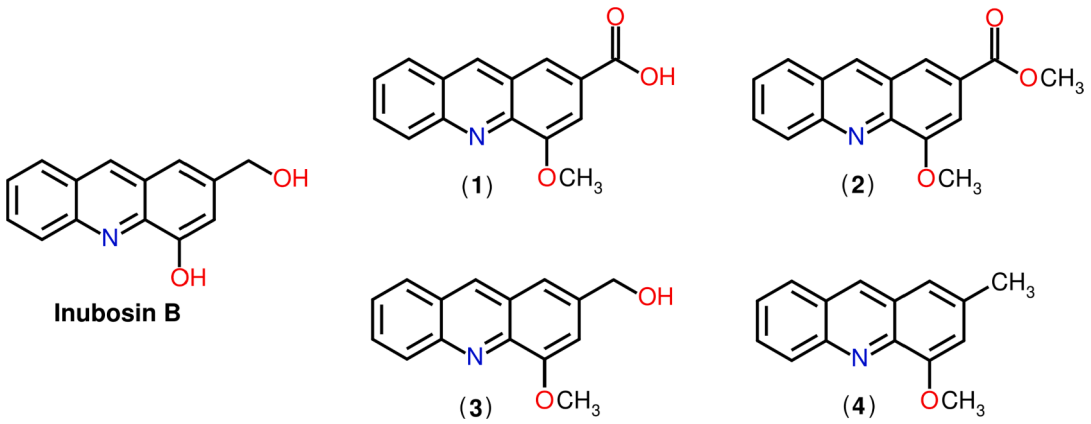

Fig. 1. Inubosin B and studied compounds **1**–**4**.

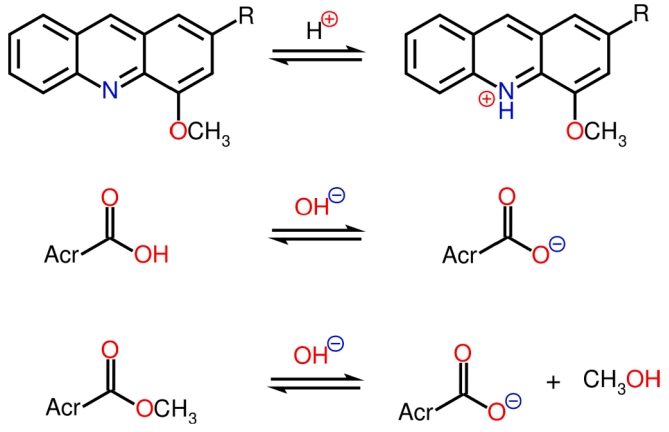

Fig. 2. Reactions studied: (top) ring protonation, general for all compounds **1**–**4**, (middle) deprotonation, for acids, (bottom) hydrolysis of methyl esters. Acr stands for 4-methoxyacridine-2-yl.

1. Introduction

Neurodegenerative diseases (NDs) are accompanied by a loss of active neurons and accumulation of misfolded proteins [1,2]. Occurrence of NDs is increasing with the aging of human population [3] and its exposition to various stress factors [4–6]. The neurons can also be damaged by various injuries [7–9].

To combat the neuronal losses, several strategies for induced neurogenesis were suggested [10,11]. Some of them aim to neurogenin 2 (Ngn2), which is a very important transcription factor for neurogenesis. In 2015, Arai et al. [12] discovered a group of acridine alkaloids – inubosins – which can increase the levels of Ngn2 and promote neural stem cell differentiation. The most active member of the inubosin family is inubosin B (Fig. 1) [12]. Together with formononetin [13] it belongs to the most powerful compounds inducing regeneration of neurons via the Ngn2 pathway.

Lately, we have developed a total synthesis of inubosin B, including four derivatives (**1**–**4**, Fig. 1) [14]. A methylation of the phenolic hydroxyl group often provides structures with enhanced biological activity [15,16]. Since all the structures **1**–**4** are potentially biologically active, their dissociation constant pK_a are of interest as they are important for the solubility and the activity [17–19]. Previously, we have also determined $pK_{a,1}$ 5.30 for the acridine ring and $pK_{a,2}$ 9.45 for the phenolic deprotonation in inubosin B [18]. In **1**–**4**, the ring protonation can occur, for the acid **1**, the carboxylate can be protonated/deprotonated as well (Fig. 2).

The constants and the titration curves can be evaluated by many means, including genetic algorithms [18,20–24]. For sets of compounds, the relationships between the acidity constants and the structures, the Hammett analysis was suggested in the past [20,25,26]. In some cases, the Hammett parameters can be predicted by DFT calculation [27].

UV–Vis spectroscopy is particularly useful to monitor heterocyclic compounds, as they usually provide a large and characteristic signal. It is useful not only for identification of the compounds but can also serve in binding studies, especially when the spectra do not interfere with other biomolecules, such as proteins, lipids, nucleic acids and saccharides [28–32]. In the past, we have shown that vibrationally resolved UV–Vis spectra of acridines can indicate the nature of the substituent at the C-9 carbon, be it C–N, C═O, or C═S group [33]. Also other laboratories found the calculations of the vibrationally resolved UV–Vis spectra useful for the polycyclic and heterocyclic compounds [34–37]. The spectral patterns, for example, are affected by explicit water solvation [38]. In DFT computations, the use of the dispersion correction was recommended for accounting for the intermolecular and intramolecular interactions [39–41]. In our analysis, we concentrate also on the HOMO-LUMO. Apart of a relation to the spectral threshold, the gap in poly-aromatic compounds was found useful for the design of organic field-effect transistors [42].

To evaluate the spectra, we explore a semi-automated processing of the titration data. An ideal spectrum for every point of the titration is obtained by a minimal square method, analyzing concentration series in sets of buffers of various *pH*, using either linear or exponential fitting. Idealized extinction coefficients are determined this way. We also studied the acidobasic and EtOAc-water phase equilibria on the basis of a genetic algorithm. For the latter, the partition coefficient could be obtained. It is shown that the vibrationally resolved spectra of the acridines are dependent on the protonation and solvation, the experimental data are analyzed using quantum-chemical and molecular dynamics calculations, environmental effects are included both via implicit and explicit solvation.

2. Material and methods

All reagents were purchased from Sigma–Aldrich–Fluka and Merck (both in Prague, Czech Republic) and used without further purification, except for drying of methanol (MeOH), toluene and tetrahydrofuran (THF). Compounds **1**–**4** were synthesized according to procedures published previously [14].

2.1 Chromatographic and MS methods

Molecular weights of compounds were determined using an electrospray ionization mass spectroscopy (ESI-MS). For HPLC, an instrument with a quaternary pump, thermostat, diode array detector and reverse-phase C_{18} columns was used. Analytical HPLC was carried out

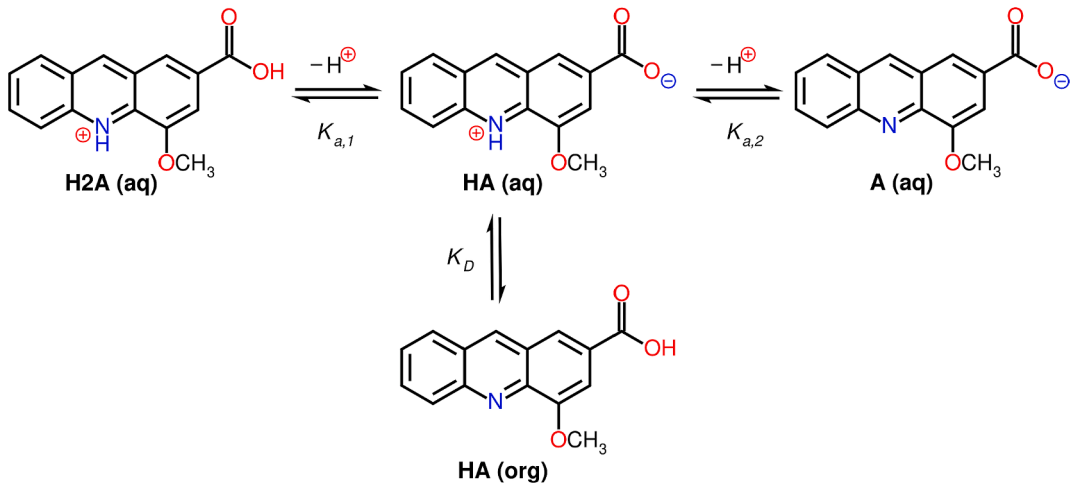

Fig. 3. Acidobasic and partition equilibria.

with a Poroshell 120 SB-C18 2.7 μm, 3.0 × 50 mm column, a flow rate 1 mL/min, and diode array detection using 5-5-100-100-5 % of ACN in 0.05 % aqueous TFA within 0-1-11-13-15 min.

2.2. Uv–vis spectra and pH titration

UV–Vis spectra for inubosin B derivatives were measured using a WTW PhotoLab7600 spectrometer. A stock solution was prepared by dissolving ca 3 mg of a compound in 2 mL of DMSO. A buffer (3 mL) of defined pH was put in 1 cm path length quartz cells, and the acridine stock solution was added stepwise, four times 2.5 μl and three times 10 μL. The spectral responses to the concentration changes were evaluated using our software (see Supplementary Information for more details). In selected cases, the extinction coefficients were evaluated manually, combining spectra at concentrations of about 15 μM, for spectral range from 200 to 300 nm, and 80 μM within 300–600 nm, using 1 nm resolution. For too low or too high pH, buffer was replaced with 1 M HCl, 0.1 M HCl, 0.01 M HCl, 0.01 M NaOH, 0.1 M NaOH, 1 M NaOH. Within 2 to 12 pH was measured by a resistant glass pH microelectrode type 01-32 (Monokrystaly, s.r.o.), outside this range, it was calculated from the concentration of H^+ ions.

2.3. Partitioning experiments

An extraction was carried out for a mixture of aqueous buffer (3 mL) and EtOAc (3 mL). Stock solution of the acid **1** (3.11 mg in 2 mL of DMSO) was added to it, either 30 μL or 80 μL for 60.8 μmol/l and 159 μmol/l solutions, respectively (Fig. S6). The system was shaken in a separatory funnel, and centrifuged using 10,000 rpm for 5 min. The centrifugation was needed to suppress scattering on contaminating droplets of other solvent. The UV–Vis spectrum was recorded and used for evaluation of the partitioning. Since the UV–Vis spectrum of the acid is dependent on *pH*, a standard of the acid in the buffer was also measured: stock solution (8 μL) + buffer (3 mL) i.e. 16.3 μmol/l.

2.4. Description of equilibria in the partition experiments

A model was proposed (Fig. 3), where three forms of the acid are expected in the water phase and one in the organic one, based on three equilibria:

$$K_{a,1} = \frac{[HA(aq)][H^+]}{[H2A]} \quad (1)$$

$$K_{a,2} = \frac{[A][H^+]}{[HA(aq)]} \quad (2)$$

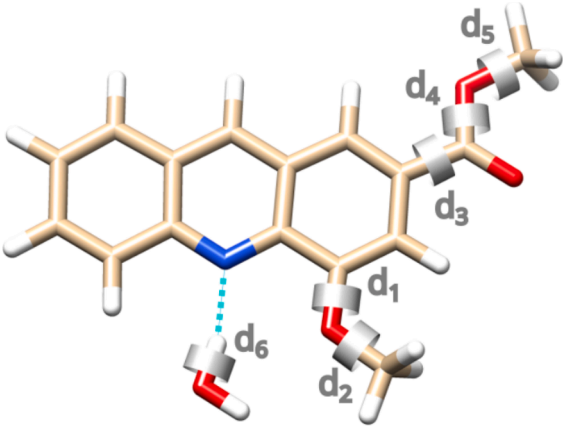

Fig. 4. Definition of studied dihedrals $\mathbf{d_1}$-$\mathbf{d_6}$.

$$K_D = \frac{[HA(org)]}{[HA(aq)]} \quad (3)$$

We derived dependencies of the absorption coefficients for acidobasic titration without extraction, water and organic phases after the extraction. For fitting the experimental data, a genetic algorithm was used [23,24], as detailed in the Supplementary Information.

2.5. Quantum chemical simulations of the spectra

The geometries of inubosin B derivatives were optimized using the Gaussian16 program [43]. The GD3BJ dispersion correction [44] was applied for all DFT calculations, to reproduce well the interactions between the ring and its substituent or environment. To map the conformer space, relaxed conformational scans were performed at the B3LYP [45]/6-31 + G**/CPCM [46,47] level (Fig. 4 and S14-S18; Tables S2–S13). For selected local minima the CAM-B3LYP [48]/6-311 + G**/CPCM level was applied, the geometry re-optimized, and UV–Vis spectra calculated at the vibronic level and at the vertical approximation. The CAM-B3LYP functional proved to be useful for similar calculation of UV–Vis spectra in the past [49]. From the calculated intensities smooth spectra were created using Gaussian bands of 25 nm full width at half height.

To understand limits of the CPCM solvent model, solvation with explicit water molecules was explored in the computations as well. For selected systems molecular dynamic was performed with the aid of the Amber14 program [50]. A cube of 4 × 4 × 4 nm^3 volume was filled with

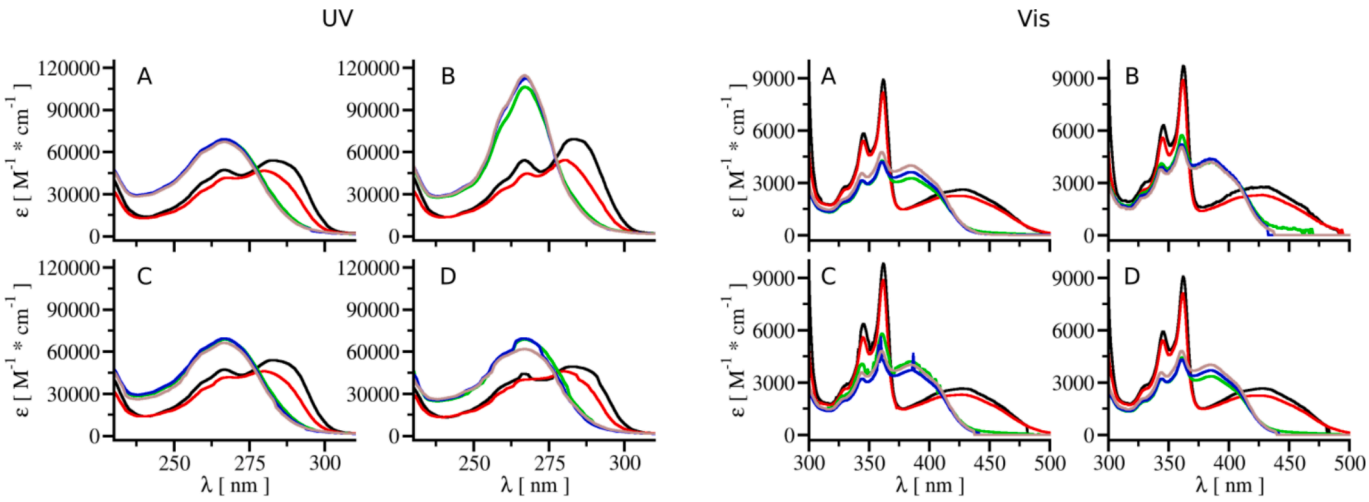

Fig. 5. UV–Vis spectra of the acid **1** obtained at pH 0, 3, 6, 8, and 14 (black, red, green, blue, and brown, respectively). Manually (A) and automatically obtained spectra (B-D) using various fitting techniques and parameters. B) Exponential fitting with maximal concentration 0.00009 mol/L, minR^2 0.9901; C) Linear fitting minR^2 0.9999; D) Linear fitting minR^2 0.9901.

the investigated acid and 2137 molecules of water, counter ions were added if needed to achieve zero charge. After an energy minimization, free dynamics was run for 47–110 ns.

The MD trajectories were analyzed using the cpptraj program of AmberTools, and a density-based clustering algorithm. First, the six closest molecules of water were considered for clustering study. The minimal number of points for a cluster was set to 10, distance cutoff for forming a cluster (ε) was set to 1.0 to 1.3 Å, sieve to frame options was on, and coordinate root-mean-squared deviation distance metric was used with sieve 5 for selected molecules from the first solvation sphere of the acridine (for the selection of appropriate ε see our previous works [51,52]).

The representative clusters with solvation of all hetero atoms in neutral and charged forms were used for further analysis. In a rapid screening, PM7 optimization of the clusters was carried out [53]; selected clusters were fully optimized at the B3LYP/6-31 + G**/CPCM level. Energies of the cluster were used to identify the most favorable solvation patterns. Cation, free base, zwitterion and anion with 6–8 water molecules (Tables S14–S18) were optimized at the CAM-B3LYP/6-31 + G**/CPCM level and vibrationally resolved spectra calculated with default parameters in Gaussian.

3. Results and discussions

3.1. Automated processing of the spectra

The processing of the spectra with home made software provided comparable results to manually processed data combining two spectra at lower and higher concentrations (Fig. 5, cf. A, C and D). The automatically generated idealized spectra are somewhat affected by the choice of

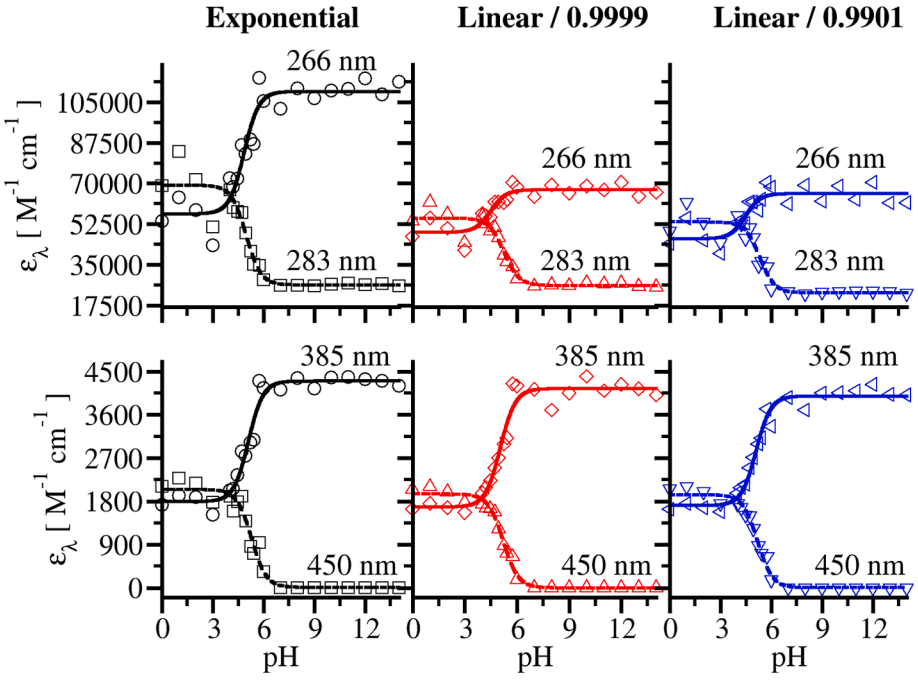

Fig. 6. Titration curves of acid (**1**) obtained from the automatically processed spectra. Black color represents exponential fitting with maximal concentration 0.00009 mol/L, minR^2 0.9901; red is for linear fitting minR^2 0.9999; and blue color is for linear fitting minR^2 0.9901.

Table 1
Dissociation constants of **1**–**4** obtained by various spectra processing methods.

Method:	Exponential minR^2 0.9901		Linear minR^2 0.9999		Linear minR^2 0.9901	
1:						
λ [nm]	**pK_a**	**R^2**	**pK_a**	**R^2**	**pK_a**	**R^2**
266	4.85	0.960	4.50	0.916	4.47	0.883
283	4.97	0.959	5.25	0.971	5.32	0.965
362	5.48	0.931	5.49	0.924	5.44	0.902
385	5.11	0.984	5.04	0.982	5.10	0.989
450	5.29	0.982	5.21	0.996	5.19	0.994
Average	5.14		5.10		5.10	
Stdev	0.25		0.37		0.38	
2:						
λ [nm]	**$pK_{a,1}$**	**$pK_{a,2}$**	**R^2**	**$pK_{a,1}$**	**$pK_{a,2}$**	**R^2**	**$pK_{a,1}$**	**$pK_{a,2}$**	**R^2**
266	–	11.95	0.991	–	11.98	0.985	–	11.98	0.979
284	3.90	12.31	0.998	4.03	12.21	0.997	4.11	12.41	0.995
362	4.09	–	0.991	4.13	–	0.984	4.01	–	0.989
385	4.08	–	0.986	4.07	–	0.987	4.02	–	0.996
450	4.16	–	0.995	4.20	–	0.999	4.18	–	0.999
Average	4.06			4.11			4.08		
Stdev	0.11			0.07			0.08		
3:						
λ [nm]	**pK_a**	**R^2**	**pK_a**	**R^2**	**pK_a**	**R^2**
258	5.12	0.939	4.99	0.959	4.98	0.950
267	4.81	0.912	5.00	0.936	4.90	0.915
359	4.99	0.957	5.02	0.961	4.93	0.976
378	4.94	0.953	4.91	0.980	4.91	0.987
429	5.09	0.959	5.01	0.978	5.00	0.975
Average	4.99		4.99		4.94	
Stdev	0.11		0.04		0.04	
4:						
259	5.24	0.977	5.06	0.982	5.02	0.986
271	4.91	0.992	5.22	0.995	5.20	0.995
361	5.21	0.989	5.20	0.994	5.13	0.992
380	5.20	0.975	5.13	0.989	5.09	0.995
433	5.11	0.974	5.20	0.979	5.14	0.985
Average	5.13		5.16		5.12	
Stdev	0.13		0.07		0.07	

the acceptable correlation coefficients (see small edges in spectra UV, D and spikes in Vis, C), e.g. for the blue spectrum UV, D, correlation coefficient of data will spontaneously rise from ca 0.9902 at 263 nm to ca 0.9996 at 264 nm. For the acid, the UV region of spectra is better processed with minR^2 equal to 0.9999, whereas the Vis region is represented nicely with minR^2 equal to 0.9901. Exponential fitting led to spectra without artifacts/discontinuity but the extinction coefficients in UV area are overestimated. Different fitting gives slightly different extinction coefficients: for instance, at 385 nm, the order of maxima from the manual processing is brown > blue > green, they are about equal for the exponential method, green > brown > blue (line, minR^2 0.9999, ignoring the spike), or brown > blue > green (line, minR^2 0.9901). However, these variations are small without significant effect on the final results.

For further validation of the method, we have measured spectra of $KMnO_4$ and compared our extinction coefficients with the published ones [54] (Fig. S5 and Table S1). Clear correspondence could be seen for peaks at 311, 508, 525 and 546 nm, bigger deviations are observed for the shoulders (Table S1). Linear methods gave average deviations 3.0 % (minR^2 0.9999) and 2.7 % (minR^2 0.9901), the exponential one about 15 % (minR^2 0.9901). Overall, as for the acid **1**, all methods provided very similar, accurate spectra.

3.2. Automated processing of titration curves

After the validation, we processed the titration data for inubosin B derivatives. For **1** (Fig. 6 and Table 1), we have selected wavelengths of 266, 283, 362, 385, and 450 nm, to capture the most significant changes. Despite the molecule having two groups potentially responding to *pH* changes (ring and acid, see Fig. 2), only the dissociation of a proton from the ring nitrogen was observed. For pK_a of the carboxylate see the section 3.3. For the ring nitrogen, almost all methods provided pK_a between 5.10 and 5.14 (Table 1). There are only small differences among fitted titration curves in the Vis region (black is close to red and blue), whereas the exponential method provides bigger changes in the spectra of different ionic states (black differs significantly from red and blue).

For the ester **2** (Fig. 7 and Table 1), we have selected wavelengths 266, 284, 362, 385, and 450 nm. Although the molecule has one group supposedly responding to *pH* changes (ring nitrogen, see Fig. 2), two transitions were visible. It turned out that the second one (pK_a around 12) was caused by a basic hydrolysis of the methyl ester group. The reaction is very fast for *pH* above 10 [55–57]. The evaluations provided pK_a between 4.06 and 4.11 (Table 1). Similarly to case of the acid, there are only small differences among titration curves obtained by various methods in the Vis region (black is close to red and blue), whereas the exponential methods provide more visible changes of the spectra for different ionic states (black differs significantly from red and blue). Interestingly, the reaction-driven transition is observable in the UV

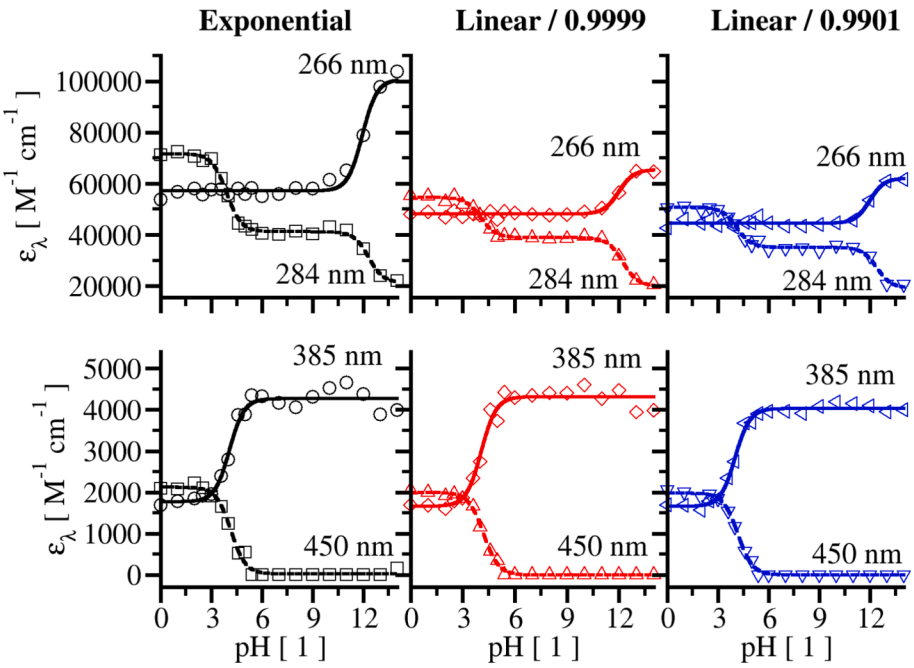

Fig. 7. Titration curves of ester (**2**) obtained from the automatically processed spectra. Black color represents exponential fitting with maximal concentration 0.00009 mol/L, minR^2 0.9901; red color serves for linear fitting minR^2 0.9999; and blue color is for linear fitting minR^2 0.9901.

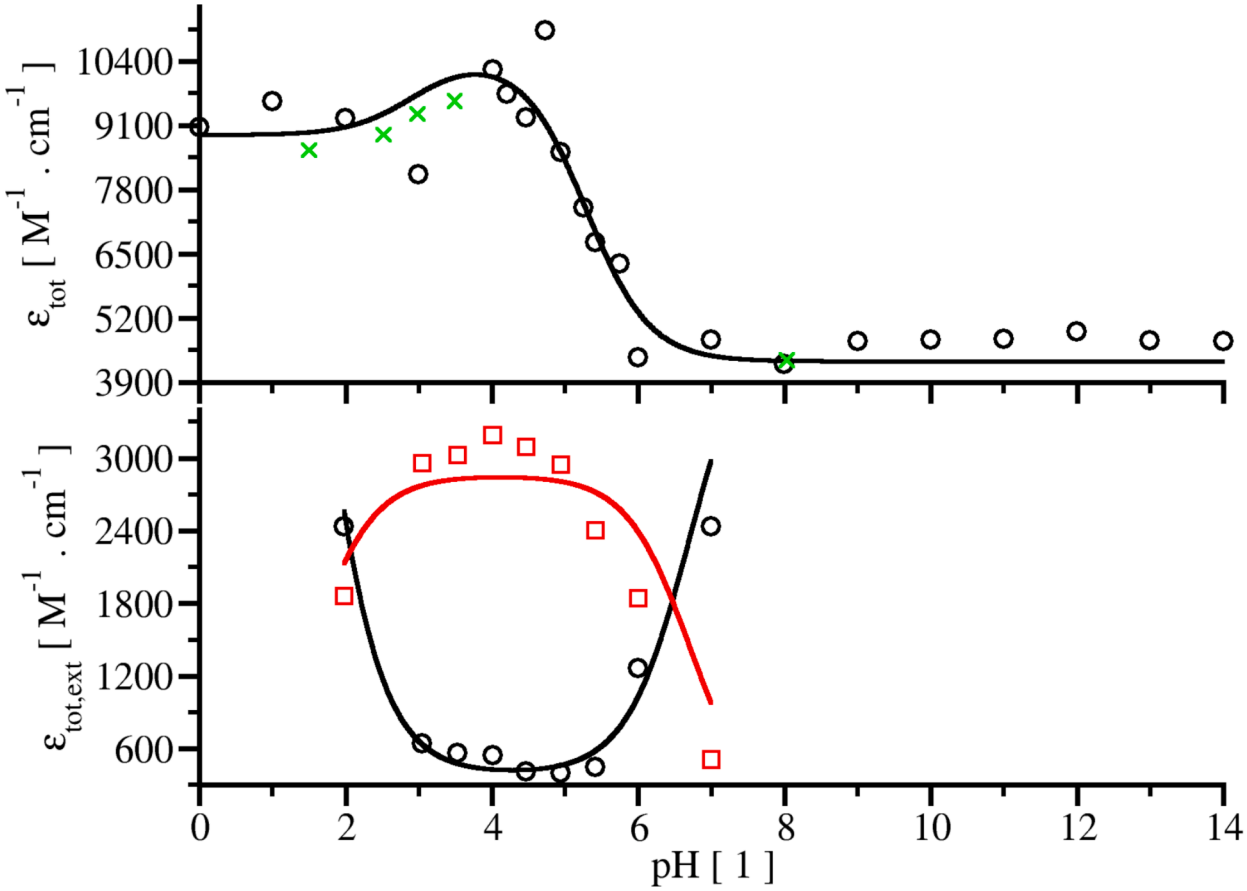

Fig. 8. Titration curves from the acidobasic and partition experiments obtained by the genetic algorithm with value of the fitness function 0.90132 (weighted average correlation coefficient). The fit parameters obtained at 362 nm were: ε_{H2A} 8902.8 $M^{-1}.cm^{-1}$, $\varepsilon_{HA\ (aq)}$ 10486.0 $M^{-1}.\ cm^{-1}$, ε_{A} 4319.4 $M^{-1}.\ cm^{-1}$, $\varepsilon_{HA\ (org)}$ 2965.9 $M^{-1}.\ cm^{-1}$, $pK_{a,1}$ 2.94, $pK_{a,2}$ 5.29, pK_D −1.41. The black curves stand for water phases, the red one for ethyl acetate. The experiments represented by the green cross × were measured after the genetic fitting, to confirm the predictions.

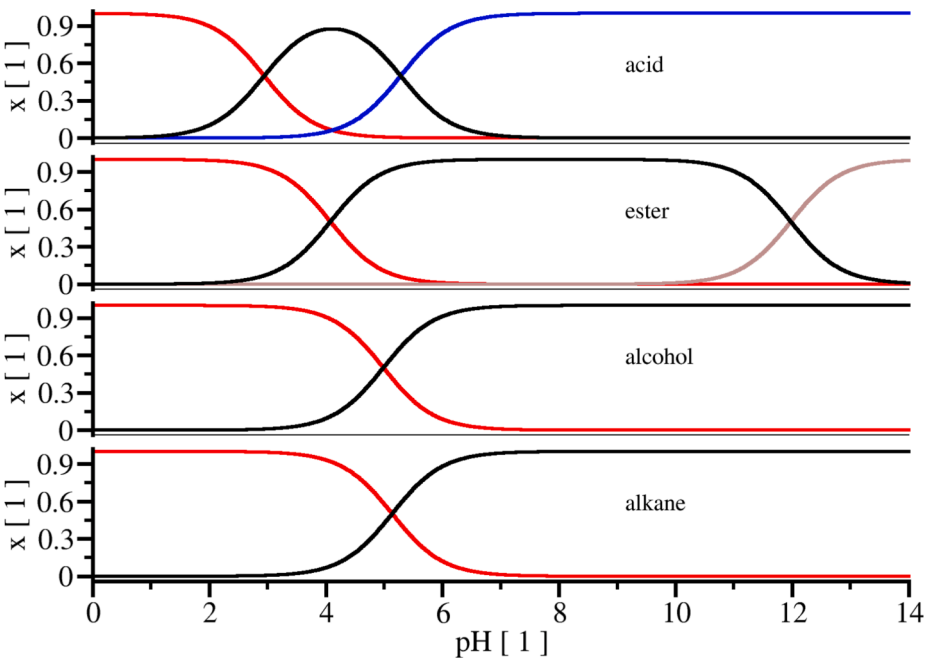

Fig. 9. Speciation charts of studied compounds. The red curves stand for the protonated forms, black ones for neutral ones, blue for anionic forms, and brown for the ester hydrolysis to the anion of the acid.

region only.

The dissociation constants of alcohol **3** and alkane **4** were obtained using the same methodology, and are tabulated in Table 1.

3.3. Distribution of the acid between water-ethyl acetate

To prove that the acid (**1**) has two ionization constants with similar values, the distribution experiment was carried out. We could see an optimal concentration, at which most of the acid is extracted by EtOAc (Fig. S6). The experiment was carried at two concentrations, a lower one for a coarse scanning, and a higher one for a fine scan. Both approaches revealed maximal concentration of the acid in EtOAc around pH 4. The UV–Vis spectra of the acid in EtOAc (Fig. S7) are not affected by the pK_a transition around pH 5. Thus, the acid exists in EtOAc as one form, most probably the neutral one. One may also assume that the concentration of the neutral form is the highest in the water phase at pH 4.

By a genetic algorithm, the equations for the equilibria were solved (Fig. 8). The first protonation occurs around pH 3. Since the extinction coefficients of the cationic and neutral molecules differ by only about 16 %, the resulting constants may be affected by the experimental noise. We also tried to monitor the titration by infrared spectroscopy (data not shown); however, bigger concentrations were needed and in the critical *pD* region of 2.5 to 6 a precipitation of the acid occurred in this case. Thus the UV–Vis titration permissible for much lower concentrations

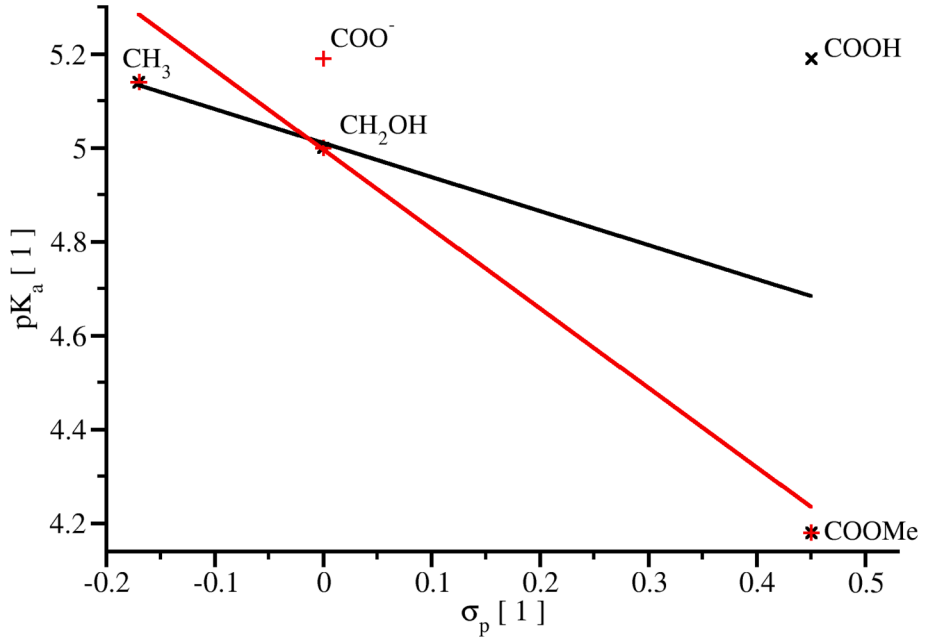

Fig. 10. The Hammett analysis of the experimental data. The carboxylic acid was evaluated either as protonated (black) or deprotonated (red). Correlation coefficients were −0.486 and −0.953 for black and red curves, respectively.

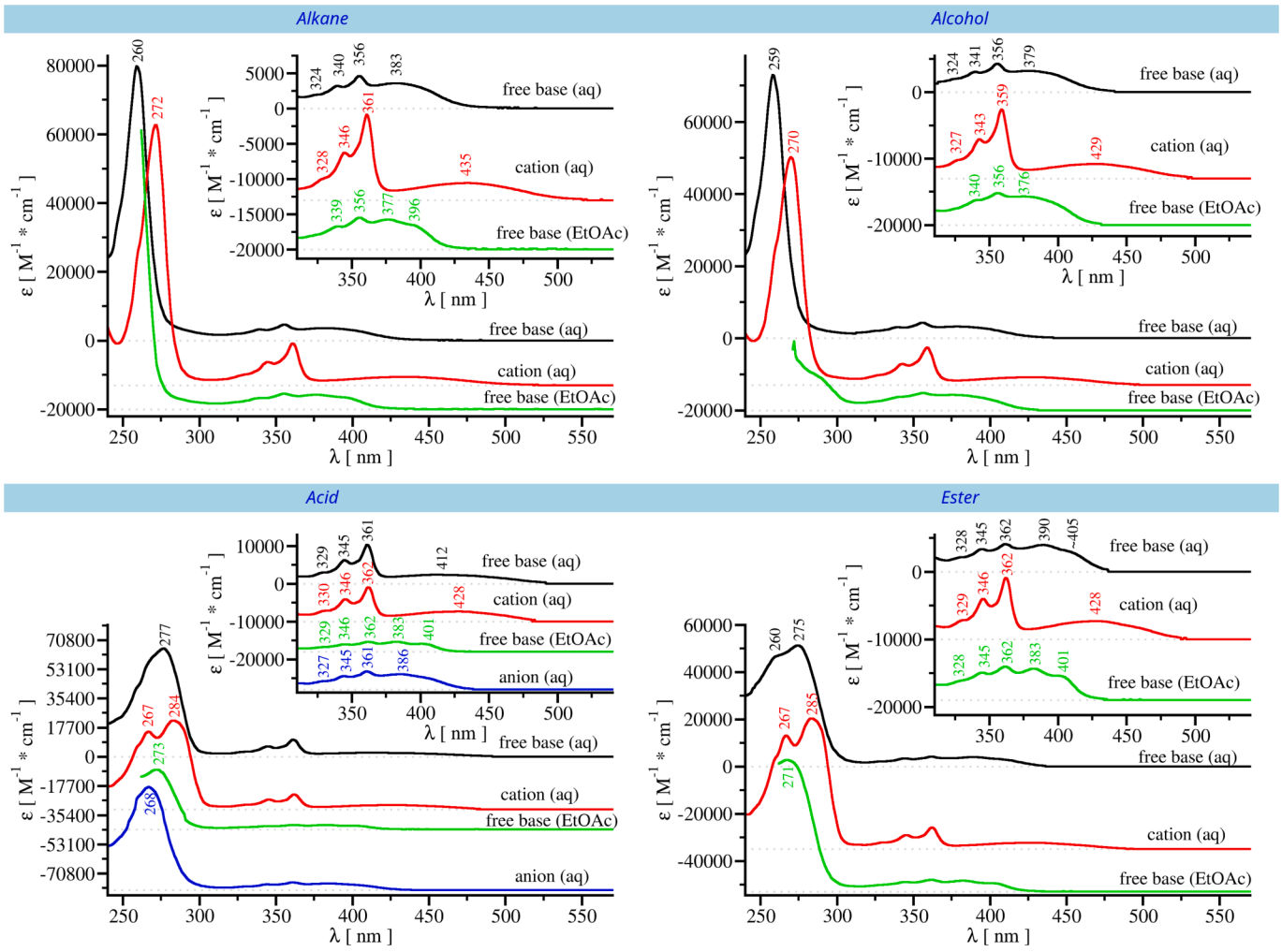

Fig. 11. Extrapolated experimental spectra, and extrapolations for individual dissociation forms of the studied compounds.

appeared more useful. Supposedly, the noise in the spectra is caused by a formation of microcrystals during the titration.

3.4. Speciation of individual forms of prepared compounds

With experimental pK_a's, speciation charts were constructed (Fig. 9; For speciation equations see Supplementary Information). From the speciation plot for the acid, it is obvious that the most efficient extraction from the water phase could be achieved at pH 4 (higher abundance of "free base"). At this *pH*, the acid is also less soluble in water. In fact, during its synthesis, it could be crystallized from water at pH 4. Sometimes, a higher *pH* around 5 is used for precipitation of **1**, since at *pH* 4, *p*-toluenesulfonic acid can co-crystallize with it. The hydrolysis of the ester is increasing with increasing *pH*. At pH 14, the spectrum of "ester" is identical to the spectrum of the anion of acid **1**, i.e. a complete hydrolysis was achieved. The knowledge of the speciation was used to obtain pure spectra of individual forms of the studied compounds.

3.5. Hammett analysis of obtained pK_a's

The pK_a's obtained were also examined in light of the Hammett theory [20,25,26]. In it, the σ_p constants describe the electronic contribution of the *para* substituent to the aromatic system. For a substituent in the *para* position to the acridine nitrogen (Fig. 10), its σ_p constant should correlate with its pK_a. For the correlation, pK_a obtained from the extinction coefficient at higher wavelengths were used (430–450 nm). The resulting Hammett function for 2-substituted 4-methoxyacridine is

$$pK_a = 5.00 - 1.69{*}\sigma_p \quad (4)$$

giving correlation coefficient of −0.953 (red function, Fig. 10).

The Hammett analysis indicates a presence of zwitterion, which is consistent with a spectroscopic analysis presented below.

3.6. Experimental UV–Vis spectra of individual forms

The extrapolated spectra of individual dissociation forms of the compounds are plotted in Fig. 11. Similarly to inubosin B [18], occasional vibrational splitting seems to be present, especially in the Vis region. The longer-wavelength part of the spectrum is very sensitive to the protonation. Here, one can also observe a solvatochromic shifts (435–428 nm in the cationic form). The deprotonation causes a blue shift by about 52, 50, 16, and, 38 nm for alkane, alcohol, acid and ester, respectively. In the acid, the blue shift can be attributed to deprotonation of the carboxylate. The subsequent deprotonation of the ring provides further 26 nm blue shift, so that the cationic and anionic forms give a shift of 42 nm (red and blue spectra), similarly to that of ester (38 nm). The presence of the carbonyl group decreases the blue shift by 10 nm, in comparison to the alkane and alcohol. For the transfer from the aqueous environment to ethyl acetate, small blue solvatochromic shifts are observed, 6, 3, 3, and 7 nm for alkane, alcohol, acid, and ester, respectively. The vibrational splitting is more pronounced in the organic

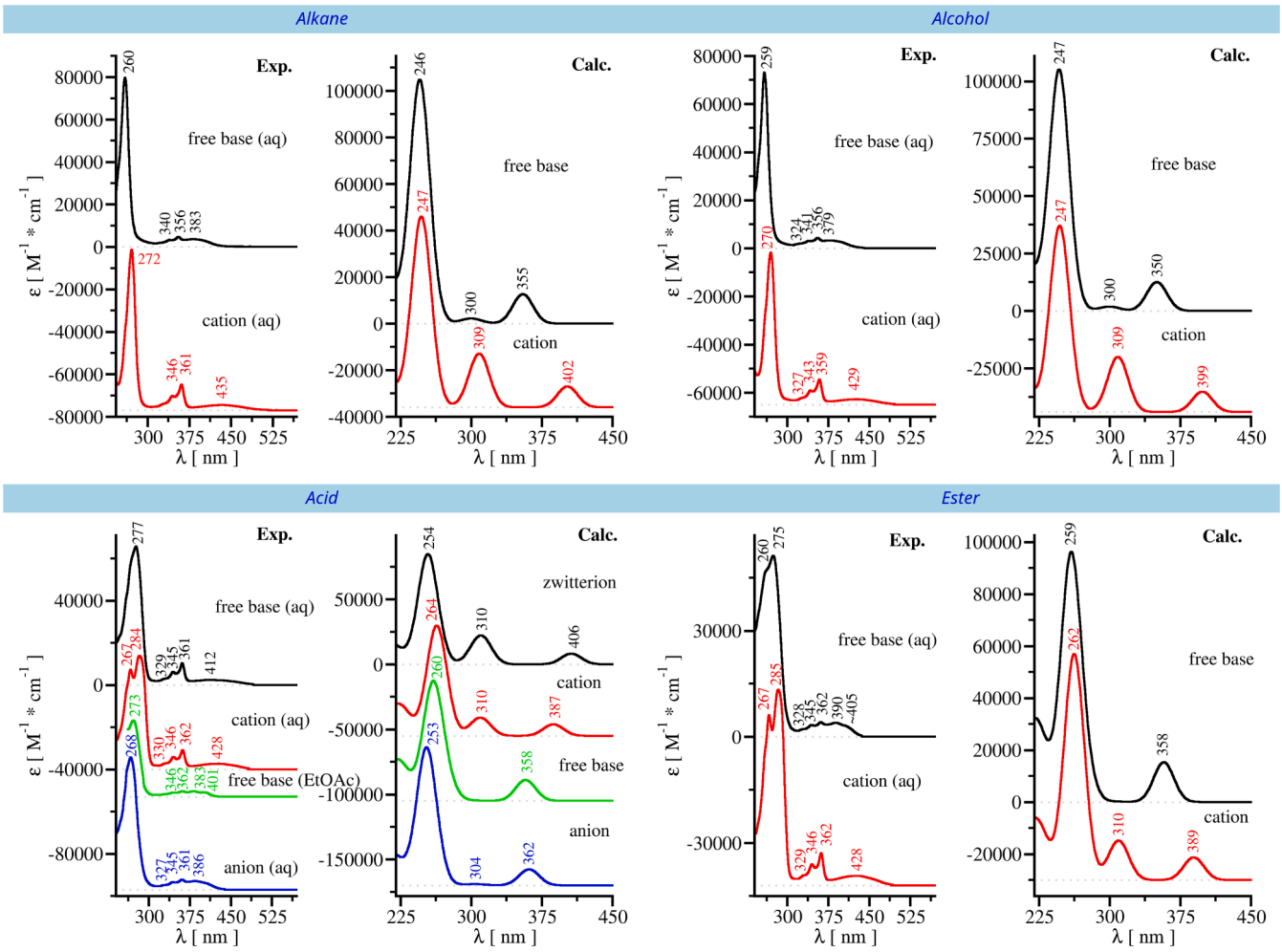

Fig. 12. Comparison of extrapolated experimental and (not vibrationally-resolved) calculated spectra of individual forms of the studied compounds.

phase than in the aqueous one.

The cationic forms of all compounds have characteristic and intense "double band" around 350 nm (red spectra, insets). This double band is much weaker in the free base and anion forms, with the exception of the acid free base (black spectrum). The spectrum of the acid free base in the aqueous solution looks differently than that in EtOAc; for the other compounds the spectra of free bases in aqueous and EtOAc solutions look similarly. Since the double band of the aqueous acid in the free base form has a shape similar to the cationic species, we can deduce a presence of the zwitterionic form, confirming the conclusion made on the basis of the blue shifts discussed above.

In addition, the bend around 270 nm appears indicative of the ring protonation. Its blue shifts caused by the deprotonation are 12 and 11 nm for alkane and alcohol, respectively. In presence of the carbonyl, intensive bands (267 and ~ 284 nm) are present in the protonated form. In aqueous free form of the acid, the bands have coalesced to 277 nm, shifted to 268 nm when the anion is made.

3.7. Calculated UV–Vis spectra

Vibrational structure in the spectra appears when the geometries of the relevant ground and excited electronic states are similar [18,34,58]. For all compounds, we could calculate the spectra without the resolution. Vibrationally-resolved spectra were obtained for some forms of **1** and **2** only; compounds **3** and **4** gave very different ground and excited states geometries.

The spectra calculated without vibrational resolution reproduced the higher intensity of the cationic band observed around 309–310 nm (Fig. 12) and the blue shift of the lowest energy band observed for the cationic to free base change. The 52 nm or 38 nm observed shifts well correspond to the 47 nm or 31 nm calculated ones for the alkane and the ester, respectively, although position of the UV band around 260 nm (e.g. alkane experiment, free base) was not reproduced well by the calculation.

In the case of the acid, the calculation is in agreement with the experiment regarding the presence of a band around 310 nm for the cation and zwitterion. For the lowest energy band and the transition from the cation to zwitterion the experimental blue shift is not reproduced. Therefore, we have considered presence of a mixture of free base and the zwitterion under the experimental conditions. For confirmation of this hypothesis, spectra of calculated free base and zwitterion were compared (Fig. S8). A 50:50 ratio can explain the experiment, e.g. a coalescence of peaks 358 nm and 406 nm is considered. This coalescence can also explain a broader experimental band of aqueous free base than that of cation. The calculated blue shift of 25 nm for cation vs anion correspond to the experimental one of 42 nm. The calculated blue shift is not bigger than that of ester, as in experiment.

The influence of the CPCM solvent model on the blue shift was examined in Fig. S9. The CPCM model could not explain the experimental blue shift when the water environment changes to ethyl acetate. Therefore, more extensive explicit hydration was applied based on the MD trajectories, PM7 pre-optimizations and TDDFT calculations. This approach had a more dramatic effect on calculated spectra (Fig. S10). Tiny reorganization of water molecules led to blue solvatochromic shift,

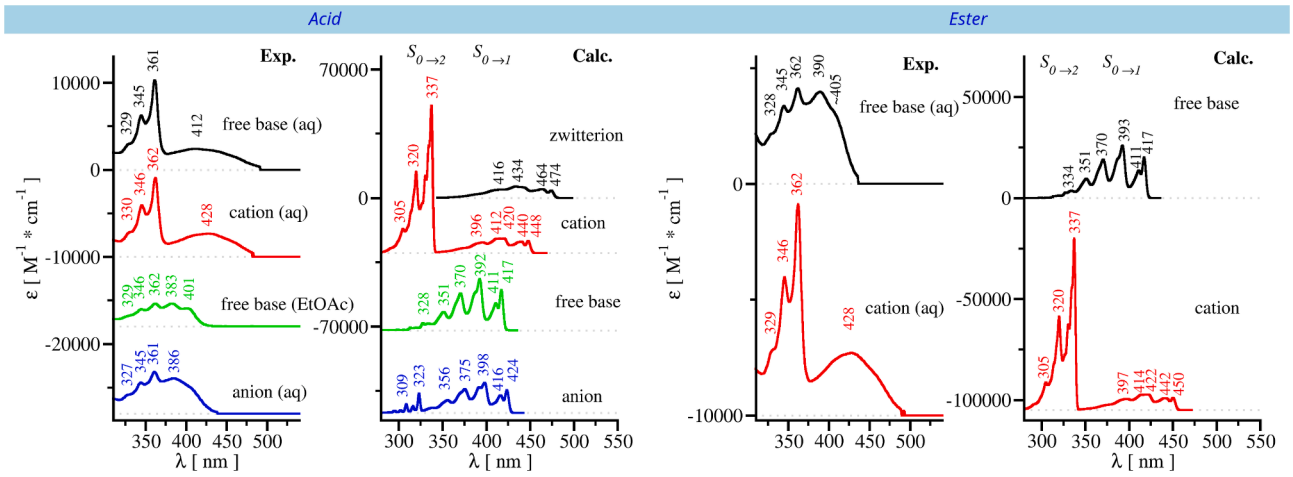

Fig. 13. Comparison of extrapolated experimental and vibrationally-resolved calculated spectra of the acid and the ester. For zwitterion, the $S_0 \rightarrow S_2$ band could not be obtained by TDDFT at this level.

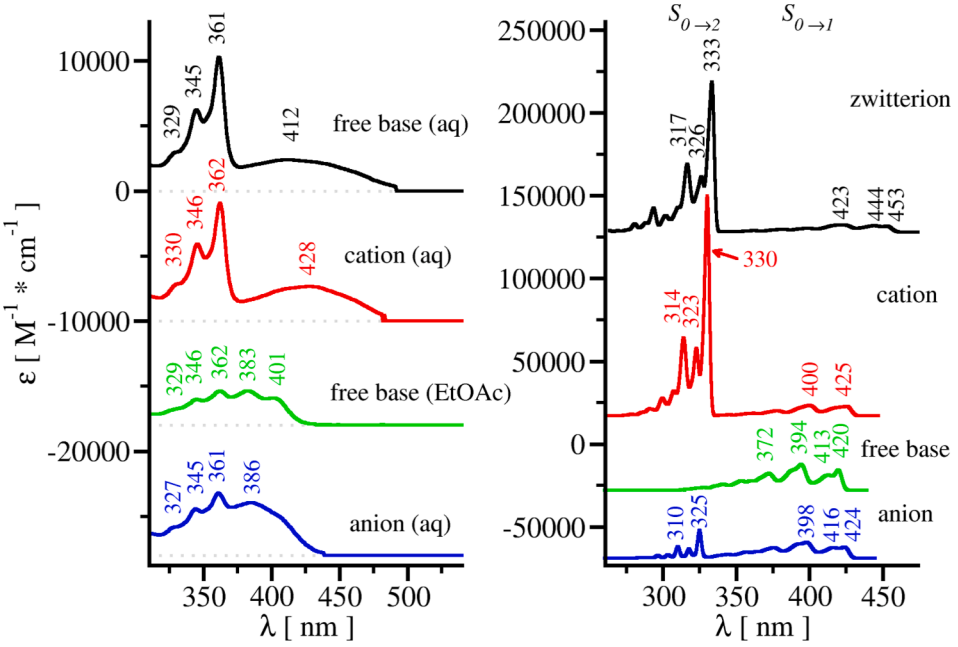

Fig. 14. Comparison of extrapolated experimental (left) and vibrationally-resolved calculated spectra of the acid (right, using explicit hydration with seven to eight molecules of water).

up to 89 nm. We can conclude that the explicit hydration is needed for full modeling of the solvatochromism.

For the UV–Vis spectra and explicitly hydrated forms, the CAM-B3LYP functional provided much better agreement with experiment than the B3LYP one (Figs. S11 and S12). This is consistent with our previous observation of iron complexes, although treated without the explicit hydration [49].

The calculations reproduced the higher intensity and vibrational splitting of the cationic band around 337 nm (Fig. 13). The band was assigned to the $S_0 \rightarrow S_2$ transition involving the HOMO–1 and LUMO orbitals. Vibronic features of this band could not be calculated for zwitterion without explicit solvation, due to instability of optimization of the second excited electronic state.

It is known that explicit solvation may be important for reproduction of the vibrationally resolved spectra with polar heteroatoms [38]. We applied the explicit solvation for acid **1**. For the clusters, optimized geometries of the ground and excited states often differed and the vibronic computation did not converge. For a limited number of the clusters, the spectra could be calculated and compared with the experimental ones (Fig. 14). By the explicit solvation, $S_0 \rightarrow S_2$ transition was reproduced for the zwitterion, similar to the cation. The $S_0 \rightarrow S_2$ intensity is very small for the free base, and the calculation reproduces the difference between the spectra obtained in water and in ethyl acetate. For the anion, the vibronic computation converged for the second most stable conformer. In our case, the explicit solvation thus gives similar results as CPCM only.

The vibrational substructure is not visible in the aqueous experiment. This is explicable by a strong water solvation and multi-conformer equilibria in water. This situation is not fully reproduced by the calculation, where only a limited number of the clusters/configurations could be included.

Selected orbitals involved in the $S_0 \rightarrow S_2$ transition are plotted in Fig. 15 and S13. Usually, HOMO-1 to LUMO and HOMO to LUMO + 1 are contributing the most. The exceptions are structures with anionic

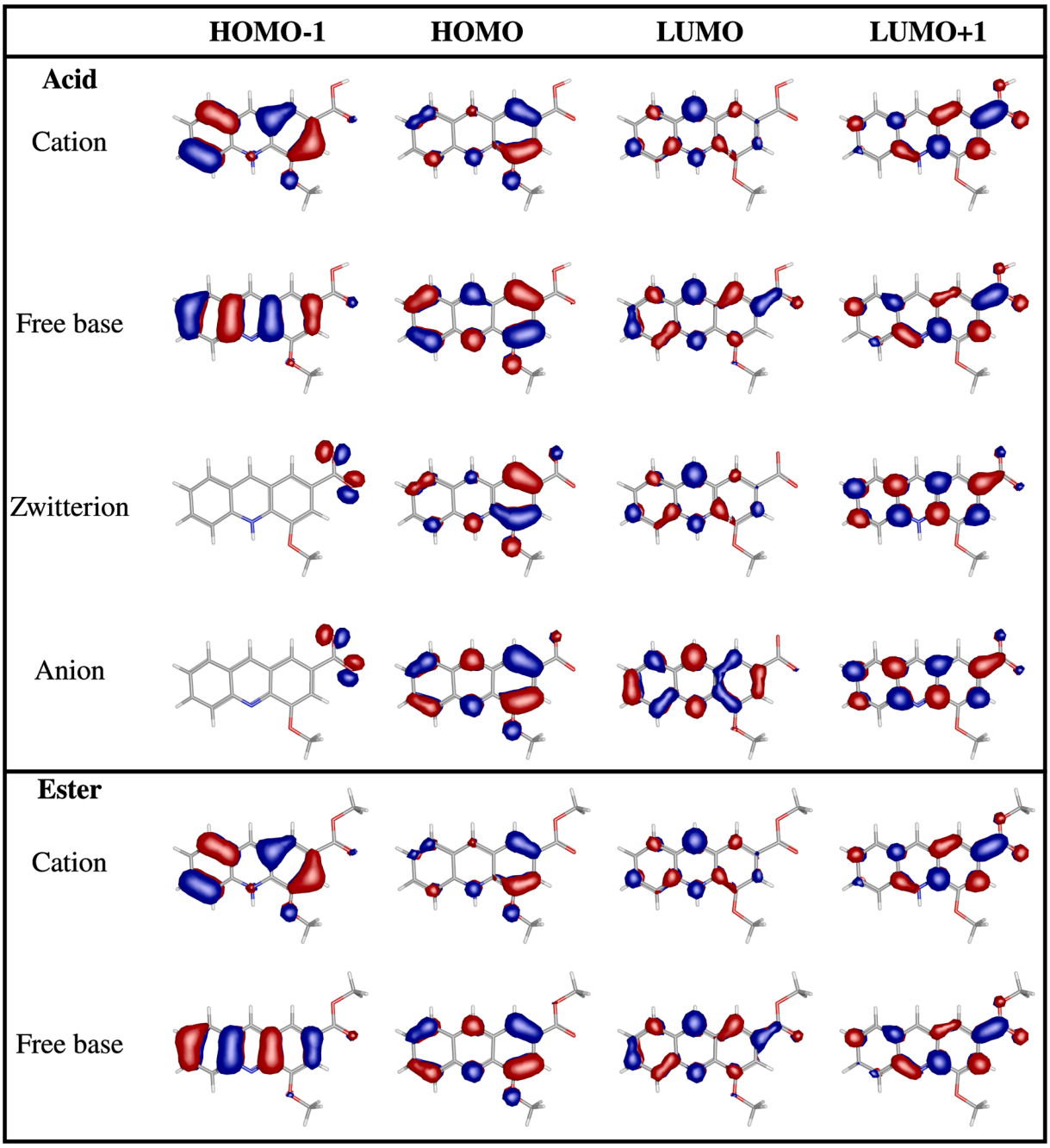

Fig. 15. Calculated HOMO-1, HOMO, LUMO, and LUMO + 1 orbitals involved in the S_1 (HOMO → LUMO) and S_2 (HOMO–1 → LUMO + HOMO → LUMO + 1) transition.

carboxylate, where transitions from HOMO-2 to LUMO and from HOMO-4 to LUMO dominate. HOMO-1 orbitals of the cation and free base cases differ significantly. A charge transfer concerning the methoxy substituent seems to play a role in the spectra. Both the HOMO and HOMO-1 orbitals of the cationic species involve the methoxy groups, whereas LUMO orbitals are elsewhere. For free bases, only HOMOs, not HOMO-1 include the methoxys.

Computed HOMO-LUMO gaps are listed in Tables S19 and S20. A change of the CPCM solvent alters the gap by less than 0.01 eV (Table S19). More significant gap changes were observed between species: change from free base to cation without carbonyl is ca 0.3–0.4 eV and with carbonyl ca 0.2 eV. In the case of acid, difference between free base and zwitterion gaps is ca 0.3 eV. Concerning HOMO-LUMO gaps, the cation is more similar to zwitterion than to free base; and anion is more similar to free base, which can be related to the similarities of the experimental spectra.

The gaps computed for the explicit hydration in Table S20 are only informative, due to the limited number of the clusters calculated. For the cations, the explicit hydration made only 0.01–0.04 eV difference compared to CPCM. In the case of the free base, the gap decreased by about 0.11 eV, for the zwitterion/anion, the gap increased/decreased by about 0.09 eV. The gaps are well-related to the experimental spectral thresholds, at 3.01 eV, 2.90 eV, and 3.21 eV for zwitterion, cation, and anion of the acid, respectively. For free bases and cations of alcohol and alkane, these are ca 3.26 eV and 2.87 eV, respectively.

4. Conclusions

Using the absorption spectroscopy and our analytical software, we determined the acidobasic constants of inubosin B derivatives and correlated their acidities with the structure using the Hammett analysis. Hammett Eq. (4) was found useful for prediction of the acidities of new inubosin derivatives. Both the TDDFT computations and experimental data indicate that the acridine acid forms zwitterion in the aqueous solution, whereas it remains without charge in the organic one. The spectra could be calculated in the vertical approximation for all studied systems, including explicitly hydrated models. By the vibronic computations further experimental spectral features could be reproduced, although the computations did not always converge, especially for the clusters. A band most characteristic for the cationic species was assigned to the $S_0 \rightarrow S_2$ transition, and the main spectral features and trends could be reproduced by the computations, both based on the vertical approximation or including the vibrational resolution. The frontier orbitals and strong calculated solvatochromism suggest that the oxygen at position 4 of the acridine ring is a key player affecting the spectra. We find these results useful for future applications of the compounds in biochemistry, as well as for a deeper analyses of the UV–Vis data.

Declaration of competing interest

The authors declare the following financial interests/personal relationships which may be considered as potential competing interests: Petr Bour reports financial support was provided by Czech Science Foundation. If there are other authors, they declare that they have no known competing financial interests or personal relationships that could have appeared to influence the work reported in this paper.

Acknowledgments

This work was supported by the Czech Science Foundation (25-15726S), Research Project RVO 61388963. Computational resources were supplied by the project "e-Infrastruktura CZ" (e-INFRA CZ LM2018140) supported by the Ministry of Education, Youth and Sports of the Czech Republic. The molecular structures were visualized using program UCSF Chimera [59].

Appendix A. Supplementary data

Supplementary data to this article can be found online at https://doi.org/10.1016/j.saa.2025.125950.

Data availability

Data will be made available on request.

References

[1] G. Tesco, S. Lomoio, Pathophysiology of neurodegenerative diseases: An interplay among axonal transport failure, oxidative stress, and inflammation? Semin. Immunol. 59 (2022) 101628 https://doi.org/10.1016/j.smim.2022.101628.
[2] G. Calabrese, C. Molzahn, T. Mayor, Protein interaction networks in neurodegenerative diseases: From physiological function to aggregation, J. Biol. Chem. 298 (2022) 102062, https://doi.org/10.1016/j.jbc.2022.102062.
[3] K. Mayne, J.A. White, C.E. McMurran, F.J. Rivera, A.G. de la Fuente, Aging and Neurodegenerative Disease: Is the Adaptive Immune System a Friend or Foe? Front. Aging Neurosci. 12 (2020) 572090 https://doi.org/10.3389/fnagi.2020.572090.
[4] K.J. Barnham, C.L. Masters, A.I. Bush, Neurodegenerative diseases and oxidative stress, Nat. Rev. Drug Dis. 3 (2004) 205–214, https://doi.org/10.1038/nrd1330.
[5] E.A. Ayeni, A.M. Aldossary, D.A. Ayejoto, L.A. Gbadegesin, A.A. Alshehri, H. A. Alfassam, H.K. Afewerky, F.A. Almughem, S.M. Bello, E.A. Tawfik, Neurodegenerative diseases: implications of environmental and climatic influences on neurotransmitters and neuronal hormones activities, Int. J. Environ. Res. Public Health 19 (2022) 12495, https://doi.org/10.3390/ijerph191912495.
[6] P. Leblanc, I.M. Vorberg, Viruses in neurodegenerative diseases: More than just suspects in crimes, PLoS Pathog. 18 (2022) e1010670, https://doi.org/10.1371/journal.ppat.1010670.
[7] R.J. Li, Z.G. Liu, Y.M. Pan, L. Chen, Z.X. Zhang, L.J. Lu, Peripheral nerve injuries treatment: a systematic review, Cell Biochem. Biophys. 68 (2014) 449–454, https://doi.org/10.1007/s12013-013-9742-1.
[8] B. Lopes, P. Sousa, R. Alvites, M. Branquinho, A.C. Sousa, C. Mendonça, L. M. Atayde, A.L. Luís, A.S.P. Varejao, A.C. Maurício, Peripheral nerve injury treatments and advances: one health perspective, Int. J. Mol. Sci. 23 (2022), https://doi.org/10.3390/ijms23020918. Art. No. 918.
[9] B.L. Sheldon, Z.T. Olmsted, S. Sabourin, E. Heydari, T.A. Harland, J.G. Pilitsis, Review of the treatments for central neuropathic pain, Brain Sci. 12 (2022), https://doi.org/10.3390/brainsci12121727. Art. No. 1727.
[10] C. Cheyuo, M. Aziz, P. Wang, Neurogenesis in neurodegenerative diseases: role of MFG-E8, Front. Neurosci. 13 (2019), https://doi.org/10.3389/fnins.2019.00569. Art. No. 569.
[11] L. Culig, X.X. Chu, V.A. Bohr, Neurogenesis in aging and age-related neurodegenerative diseases, Ageing Res. Rev. 78 (2022) 101636, https://doi.org/10.1016/j.arr.2022.101636.
[12] M.A. Arai, K. Koryudzu, M. Ishibashi, Inubosins A, B, and C Are acridine alkaloids isolated from a culture of *Streptomyces* sp IFM 11440 with Ngn2 promoter activity, J. Nat. Prod. 78 (2015) 311–314, https://doi.org/10.1021/np5006218.
[13] M.A. Arai, K. Koryudzu, T. Koyano, T. Kowithayakorn, M. Ishibashi, Naturally occurring Ngn2 promoter activators from *Butea superba*, Mol. Biosys. 9 (2013) 2489–2497, https://doi.org/10.1039/c3mb70083f.
[14] M.F. Hamissa, P. Niederhafner, M. Safarík, M. Telus, L. Kolárová, L. Koutná, H. Sestáková, R. Soucek, J. Sebestík, Total synthesis of inubosin B, Tetrahedron Lett. 61 (2020) 152641, https://doi.org/10.1016/j.tetlet.2020.152641.
[15] J. Sebestík, S.M. Marques, P.L. Falé, S. Santos, D.M. Arduíno, S.M. Cardoso, C. R. Oliveira, M.L.M. Serralheiro, M.A. Santos, Bifunctional phenolic-choline conjugates as anti-oxidants and acetylcholinesterase inhibitors, J. Enzyme Inhib. Med. Chem. 26 (2011) 485–497, https://doi.org/10.3109/14756366.2010.529806.
[16] G. Li, M.L. Lou, X.B. Qi, A brief overview of classical natural product drug synthesis and bioactivity, Org. Chem. Front. 9 (2022) 517–571, https://doi.org/10.1039/d1qo01341f.
[17] D.T. Manallack, R.J. Prankerd, E. Yuriev, T.I. Oprea, D.K. Chalmers, The significance of acid/base properties in drug discovery, Chem. Soc. Rev. 42 (2013) 485–496, https://doi.org/10.1039/c2cs35348b.
[18] M.F. Hamissa, P. Niederhafner, H. Sestáková, M. Safarík, R. Hadravová, J. Sebestík, Neutral and charged forms of inubosin B in aqueous solutions at different pH and on the surface of Ag nanoparticles, J. Mol. Struct. 1250 (2022) 131828, https://doi.org/10.1016/j.molstruc.2021.131828.
[19] D. Krajcar, R. Jereb, I. Legen, J. Opara, I. Grabnar, Predictive potential of acido-basic properties, solubility and food on bioequivalence study outcome: analysis of 128 studies, Drugs R&D 23 (2023) 211–220, https://doi.org/10.1007/s40268-023-00426-6.
[20] J.W. Tomsho, A. Pal, D.G. Hall, S.J. Benkovic, Ring structure and aromatic substituent effects on the p*K*a of the benzoxaborole pharmacophore, ACS Med. Chem. Lett. 3 (2012) 48–52, https://doi.org/10.1021/ml200215j.
[21] L.J. Reed, J. Berkson, The application of the logistic function to experimental data, J. Phys. Chem. 33 (1929) 760–779, https://doi.org/10.1021/j150299a014.
[22] C.W. Eaker, Fitting and analyzing pH titration curves on a graphing calculator, Chem. Educ. 5 (2000) 329–334, https://doi.org/10.1007/s00897000426a.
[23] M. Gulsen, A.E. Smith, D.M. Tate, A genetic algorithm approach to curve-fitting, Int. J. Prod. Res. 33 (1995) 1911–1923, https://doi.org/10.1080/00207549508904789.
[24] G.M. Morris, D.S. Goodsell, R.S. Halliday, R. Huey, W.E. Hart, R.K. Belew, A. J. Olson, Automated docking using a Lamarckian genetic algorithm and an empirical binding free energy function, J. Comput. Chem. 19 (1998) 1639–1662, https://doi.org/10.1002/(SICI)1096-987X(19981115)19:14<1639::AID-JCC10>3.0.CO;2-B.
[25] J. Jian, J. Poater, R. Hammink, P. Tinnemans, C.J. McKenzie, F.M. Bickelhaupt, J. Mecinovic, Through-space polar-π interactions in 2,6-diarylthiophenols, ChemPhysChem 21 (2020) 1092–1100, https://doi.org/10.1002/cphc.202000132.
[26] C. Hansch, A. Leo, R.W. Taft, A survey of Hammett substituent constants and resonance and field parameters, Chem. Rev. 91 (1991) 165–195, https://doi.org/10.1021/cr00002a004.
[27] G.D. Stroscio, N. Goldman, Univariate prediction of hammett parameters and select relative reaction rates using loewdin atomic charges, J. Phys. Chem. A 129 (2024) 356–366, https://doi.org/10.1021/acs.jpca.4c05805.
[28] T. Biver, Use of UV-Vis spectrometry to gain information on the mode of binding of small molecules to DNAs and RNAs, Appl. Spect. Rev. 47 (2012) 272–325, https://doi.org/10.1080/05704928.2011.641044.
[29] J. Sebestík, I. Stibor, J. Hlavácek, New peptide conjugates with 9-aminoacridine:: synthesis and binding to DNA, J. Pept. Sci. 12 (2006) 472–480, https://doi.org/10.1002/psc.752.
[30] J. Plsikova, L. Janovec, J. Koval, J. Ungvarsky, J. Mikes, R. Jendzelovsky, P. Fedorocko, J. Imrich, P. Kristian, J. Kasparkova, V. Brabec, M. Kozurkova, 3,6-Bis(3-alkylguanidino)acridines as DNA-intercalating antitumor agents, Eur. J. Med. Chem. 57 (2012) 283–295, https://doi.org/10.1016/j.ejmech.2012.09.020.
[31] T. Suzuki, Y. Kuroda, K. Wada, Y. Sakano, R. Katoono, K. Fujiwara, F. Kakiuchi, T. Fukushima, Oxidative protonolysis of the expanded central C-C bond in a Di (spiroacridan)-type hexaphenylethane derivative accompanied by UV- vis, FL, and CD spectral changes, Chem. Lett. 43 (2014) 887–889, https://doi.org/10.1246/cl.140192.
[32] M. Safarík, T. Mosko, Z. Zawada, E. Safaríková, M. Dracínsky, K. Holada, J. Sebestík, Reactivity of 9-aminoacridine drug quinacrine with glutathione limits

its antiprion activity, Chem. Biol. Drug Des. 89 (2017) 932–942, https://doi.org/10.1111/cbdd.12918.
[33] Z. Zawada, M. Safarík, E. Dvoráková, O. Janousková, A. Brezinová, I. Stibor, K. Holada, P. Bour, J. Hlavácek, J. Sebestík, Quinacrine reactivity with prion proteins and prion-derived peptides, Amino Acids 44 (2013) 1279–1292, https://doi.org/10.1007/s00726-013-1460-x.
[34] V. Barone, J. Bloino, M. Biczysko, F. Santoro, Fully integrated approach to compute vibrationally resolved optical spectra: from small molecules to macrosystems, J. Chem. Theory Comput. 5 (2009) 540–554, https://doi.org/10.1021/ct8004744.
[35] R. Rüger, T. Niehaus, E. van Lenthe, T. Heine, L. Visscher, Vibrationally resolved UV/Vis spectroscopy with time-dependent density functional based tight binding, J. Chem. Phys. 145 (2016) 184102, https://doi.org/10.1063/1.4966918.
[36] I. Benkyi, E. Tapavicza, H. Fliegl, D. Sundholm, Calculation of vibrationally resolved absorption spectra of acenes and pyrene, Phys. Chem. Chem. Phys. 21 (2019) 21094–21103, https://doi.org/10.1039/c9cp04178h.
[37] R.J. Chadwick, K. Wickham, N.A. Besley, Simulation of vibrationally resolved absorption spectra of neutral and cationic polyaromatic hydrocarbons, Theor. Chem. Acc. 139 (2020), https://doi.org/10.1007/s00214-020-02697-7. Art. No. 185.
[38] E.S. Savenko, V.V. Kostjukov, Contributions of conformations, vibronic coupling, and hydration to photoexcitation of coumarin 334 in aqueous solution, Chem. Pap. 76 (2022) 6567–6578, https://doi.org/10.1007/s11696-022-02357-z.
[39] M.O. Hight, J.Y. Wong, A.E. Pimentel, T.A. Su, Intramolecular London dispersion interactions in single-molecule junctions, J. Am. Chem. Soc. 146 (2024) 4716–4726, https://doi.org/10.1021/jacs.3c12183.
[40] R. Lonsdale, J.N. Harvey, A.J. Mulholland, Effects of dispersion in density functional based quantum mechanical/molecular mechanical calculations on cytochrome P450 catalyzed reactions, J. Chem. Theory Comput. 8 (2012) 4637–4645, https://doi.org/10.1021/ct300329h.
[41] M. Bursch, J.M. Mewes, A. Hansen, S. Grimme, Best-practice DFT protocols for basic molecular computational chemistry, Angew. Chem. Int. Ed. 61 (2022), https://doi.org/10.1002/anie.202205735. Art. No. e202205735.
[42] A. Pareek, M.Y. Mehboob, M. Cieplak, M. Majdecki, H. Szabat, K. Noworyta, P. Polczynski, M. Morawiak, P.S. Sharma, C. Foroutan-Nejad, P. Gawel, Indoloindolizines: the complete story of a polycyclic aromatic scaffold from theoretical design to organic field-effect transistor applications, J. Am. Chem. Soc. (2025), https://doi.org/10.1021/jacs.4c16189.
[43] M.J. Frisch, G.W. Trucks, H.B. Schlegel, G.E. Scuseria, M.A. Robb, J.R. Cheeseman, G. Scalmani, V. Barone, G.A. Petersson, H. Nakatsuji, X. Li, M. Caricato, A.V. Marenich, J. Bloino, B.G. Janesko, R. Gomperts, B. Mennucci, H.P. Hratchian, J.V. Ortiz, A.F. Izmaylov, J.L. Sonnenberg, Williams, F. Ding, F. Lipparini, F. Egidi, J. Goings, B. Peng, A. Petrone, T. Henderson, D. Ranasinghe, V.G. Zakrzewski, J. Gao, N. Rega, G. Zheng, W. Liang, M. Hada, M. Ehara, K. Toyota, R. Fukuda, J. Hasegawa, M. Ishida, T. Nakajima, Y. Honda, O. Kitao, H. Nakai, T. Vreven, K. Throssell, J.A. Montgomery Jr, J.E. Peralta, F. Ogliaro, M.J. Bearpark, J.J. Heyd, E. N. Brothers, K.N. Kudin, V.N. Staroverov, T.A. Keith, R. Kobayashi, J. Normand, K. Raghavachari, A.P. Rendell, J.C. Burant, S.S. Iyengar, J. Tomasi, M. Cossi, J.M. Millam, M. Klene, C. Adamo, R. Cammi, J.W. Ochterski, R.L. Martin, K. Morokuma, O. Farkas, J.B. Foresman, D.J. Fox, Gaussian 16 Rev. C.01, Wallingford, CT (2016).
[44] S. Grimme, S. Ehrlich, L. Goerigk, Effect of the Damping Function in Dispersion Corrected Density Functional Theory, J. Comput. Chem. 32 (2011) 1456–1465, https://doi.org/10.1002/jcc.21759.
[45] A.D. Becke, Density-functional thermochemistry III. The role of exact exchange, J. Chem. Phys. 98 (1993) 5648–5652, https://doi.org/10.1063/1.464913.
[46] J. Tomasi, B. Mennucci, R. Cammi, Quantum mechanical continuum solvation models, Chem. Rev. 105 (2005) 2999–3093, https://doi.org/10.1021/cr9904009.
[47] A. Klamt, G. Schuurmann, COSMO – a new approach to dielectric screening in solvents with explicit expressions for the screening energy and its gradient, J. Chem. Soc. Perkin Trans. 2 (1993) 799–805, https://doi.org/10.1039/p29930000799.
[48] T. Yanai, D.P. Tew, N.C. Handy, A new hybrid exchange-correlation functional using the Coulomb-attenuating method (CAM-B3LYP), Chem. Phys. Lett. 393 (2004) 51–57, https://doi.org/10.1016/j.cplett.2004.06.011.
[49] J. Sebestík, M. Safarík, P. Bour, Ferric complexes of 3-hydroxy-4-pyridinones characterized by density functional theory and Raman and UV-Vis spectroscopies, Inorg. Chem. 51 (2012) 4473–4481, https://doi.org/10.1021/ic202004d.
[50] D.A. Case, V. Babin, J.T. Berryman, R.M. Betz, Q. Cai, D.S. Cerutti, T.E. Cheatham, T.A. Darden, R.E. Duke, H. Gohlke, A.W. Goetz, S. Gusarov, N. Homeyer, P. Janowski, J. Kaus, I. Kolossváry, A. Kovalenko, T.S. Lee, S. LeGrand, T. Luchko, R. Luo, B. Madej, K.M. Merz, F. Paesani, D.R. Roe, A. Roitberg, C. Sagui, R. Salomon-Ferrer, G. Seabra, C.L. Simmerling, W. Smith, J. Swails, R.C. Walker, J. Wang, R.M. Wolf, X. Wu, P.A. Kollman, AMBER 14, University of California, San Francisco, 2014.
[51] P. Niederhafner, M. Safarík, J. Neburková, T.A. Keiderling, P. Bour, J. Sebestík, Monitoring peptide tyrosine nitration by spectroscopic methods, Amino Acids 53 (2021) 517–532, https://doi.org/10.1007/s00726-020-02911-7.
[52] M. Beresová, J. Bufka, M. Safarík, P. Bour, J. Sebestík, Conformations and hydration of halopropionic acids studied by molecular dynamics and Raman optical activity, Spectrochim. Acta A Mol. Biomol. Spectrosc. 309 (2024) 123852, https://doi.org/10.1016/j.saa.2024.123852.
[53] J.J.P. Stewart, Optimization of parameters for semiempirical methods VI: more modifications to the NDDO approximations and re-optimization of parameters, J. Mol. Model. 19 (2013) 1–32, https://doi.org/10.1007/s00894-012-1667-x.
[54] G. Den Boef, H.J. van der Beek, Th. Braaf, Absorption spectra in the visible and U. V. region of potassium permanganate and potassium manganate in solution and their application to the analysis of mixtures of these compounds, Recl. Trav. Chim. Pays-bas 77 (1958) 1064–1070, https://doi.org/10.1002/recl.19580771110.
[55] F. Esteve, T. Rieu, J.M. Lehn, Constitutional adaptation to p*K*a modulation by remote ester hydrolysis, Chem. Sci. 15 (2024) 7092–7103, https://doi.org/10.1039/d4sc01288g.
[56] P. Minazzi, L. Lattuada, I.G. Menegotto, G.B. Giovenzana, An enzymatic approach to bifunctional chelating agents, Org. Biomol. Chem. 12 (2014) 6915–6921, https://doi.org/10.1039/c4ob00810c.
[57] R.M. Smith, D.E. Hansen, The pH-rate profile for the hydrolysis of a peptide bond, J. Am. Chem. Soc. 120 (1998) 8910–8913, https://doi.org/10.1021/ja9804565.
[58] F. Santoro, A. Lami, R. Improta, J. Bloino, V. Barone, Effective method for the computation of optical spectra of large molecules at finite temperature including the Duschinsky and Herzberg-Teller effect: The Qx band of porphyrin as a case study, J. Chem. Phys. 128 (2008) 224311, https://doi.org/10.1063/1.2929846.
[59] E.F. Pettersen, T.D. Goddard, C.C. Huang, G.S. Couch, D.M. Greenblatt, E.C. Meng, T.E. Ferrin, UCSF chimera – a visualization system for exploratory research and analysis, J. Comput. Chem. 25 (2004) 1605–1612, https://doi.org/10.1002/jcc.20084.